

On the long-term evolution of razor-thin galactic discs: Bailescu–Lenard prediction and perspectives

Mathieu Roule¹, Jean-Baptiste Fouvry¹, Christophe Pichon^{1, 2, 3*}, and Pierre-Henri Chavanis⁴

¹ Institut d’Astrophysique de Paris, CNRS and Sorbonne Université, UMR 7095, 98 bis Boulevard Arago, F-75014 Paris, France

² IPhT, DRF-INP, UMR 3680, CEA, L’Orme des Merisiers, Bât 774, 91191 Gif-sur-Yvette, France

³ Kyung Hee University, Dept. of Astronomy & Space Science, Yongin-shi, Gyeonggi-do 17104, Republic of Korea

⁴ Laboratoire de Physique Théorique, Université de Toulouse, CNRS, UPS, France

February 12, 2025

ABSTRACT

In the last five decades, numerical simulations have provided invaluable insights into the evolution of galactic discs over cosmic times. As a complementary approach, developments in kinetic theory now also offer a theoretical framework to understand statistically their long-term evolution. The current state-of-the-art kinetic theory of isolated stellar systems is the inhomogeneous Bailescu–Lenard equation. It can describe the long-term evolution of a self-gravitating razor-thin disc under the effect of resonant interactions between collectively amplified noise-driven fluctuations. In this work, confronting theoretical predictions to numerical simulations, we quantitatively show that kinetic theory indeed captures the average long-term evolution of cold stellar discs. Leveraging the versatility of kinetic methods, we then offer some new perspectives on this problem, namely (i) the crucial impact of collective effects in accelerating the relaxation; (ii) the role of (weakly) damped modes in shaping the disc’s orbital heating; (iii) the bias introduced by gravitational softening on long timescales; (iv) the resurgence of strong stochasticity near marginal stability. These elements call for an appropriate choice of softening kernel when simulating the long-term evolution of razor thin discs and for an extension of kinetic theory beyond the average evolution. Notwithstanding, kinetic theory captures quantitatively the ensemble-averaged long-term response of such discs.

Key words. Diffusion - Gravitation - Galaxies: kinematics and dynamics - Galaxies: discs

1. Introduction

Kinetic theory aims at describing statistically the evolution of many-body systems over long timescales. This endeavour is timely given the wealth of observational data recently available, e.g., GAIA (Gaia Collaboration et al. 2016) that offers an unprecedented view on the dynamical state of the Milky Way (see, e.g., Trick et al. 2019; Hunt et al. 2019), as well as large surveys such as JWST (Gardner et al. 2006) that give access to samples of galaxies with various morphological types across cosmic times (Kuhn et al. 2024). To leverage this statistical sample of galactic observations, the goal of kinetic theory is to capture their long-term evolution via a “collision operator” that describes quantitatively these system’s mean relaxation, i.e., the dynamical rearrangement of their orbital distribution. We refer to Chavanis (2013, 2024) for a thorough historical account on kinetic theory applied to self-gravitating systems. In this work, we will focus on the use of kinetic theory to describe the self-induced relaxation of galactic discs, a key ingredient of their morphological transformation.

If one’s goal is to describe the long-term evolution of a stellar disc, a few key properties must be accounted for. First, galactic discs are spatially *inhomogeneous*, i.e., stars follow intricate orbits, as described by angle-action coordinates (Binney & Tremaine 2008). Second, galactic discs are *resonant*, i.e., stellar orbits may resonate with one another, e.g., to source dynamical friction (Lynden-Bell & Kalnajs 1972). Third, galactic discs are *self-gravitating*, i.e., discs strongly enhance perturbations, e.g.,

through swing amplification arising from collective effects (Julian & Toomre 1966). Fourth, galactic discs are *discrete*, i.e., they are composed of a finite number of constituents, hence unavoidably submitted to an intrinsic Poisson fluctuations.

It is only recently that a fully self-consistent kinetic theory managed to take into account all these defining features. It is the celebrated *inhomogeneous Bailescu–Lenard equation* (Heyvaerts 2010; Chavanis 2012). This kinetic equation fully embraces spatial inhomogeneity to describe the average long-term impact of resonantly-coupled, collectively amplified and internally-driven fluctuations on the orbital distribution of a stellar system. Phrased differently, this master equation, on paper at least, encompasses all the key dynamical properties of isolated stellar discs. Since its derivation, this equation has been successfully and quantitatively applied to various systems such as the Hamiltonian mean field (HMF) model (Benetti & Marcos 2017), galactic nuclei (Fouvry & Bar-Or 2018), globular clusters (Fouvry et al. 2021) and one-dimensional gravity (Roule et al. 2022). Yet its validation on cold galactic discs has remained qualitative at best (Fouvry et al. 2015).

This paper addresses two key questions regarding the fate of isolated stellar discs: (i) How do resonant interactions and collective effects shape the long-term evolution of stellar discs? (ii) What are the limitations of kinetic theories in predicting the evolution of these cold self-gravitating systems? For that purpose, we study the Mestel disc (Zang 1976) as the testbed of kinetic theory.

This paper is organised as follows. Section 2 presents the disc model we consider and reviews previous works. Section 3 then

* Corresponding author: pichon@iap.fr

considers the disc’s averaged long-term evolution as measured in N -body simulations and predicted by the Balescu–Lenard (BL) equation. Section 4 discusses in turn the impact of self-gravity, damped modes, softening and long-term stochasticity near phase transition. Finally, section 5 wraps up and offers some perspectives for future investigations. Throughout the main text, technical details are kept to a minimum and deferred to Appendices or to relevant references.

2. Model and earlier results

2.1. Razor-thin disc model

We focus on tapered Mestel discs (Mestel 1963), whose dynamics has been extensively studied (e.g., Zang 1976; Toomre 1981; Evans & Read 1998; Sellwood & Evans 2001; Sellwood 2012; Fouvry et al. 2015). A razor-thin Mestel disc has constant circular velocity, V_0 , to mimic the (relatively) flat rotation curve of the Milky Way (see, e.g., Eilers et al. 2019). The associated potential is

$$\psi(r) = V_0^2 \ln(r/R_0), \quad (1)$$

which sets the dynamical time to $t_{\text{dyn}} = V_0/R_0$. In the following, we work within the units $G = R_0 = V_0 = 1$. Mestel discs have infinite mass and their orbital frequencies diverge like $1/r$ in the centre.¹ A compatible distribution function (DF) for a Mestel disc is given by (see, e.g., Chakrabarty 2004)

$$F(E, L) = C L^q e^{-E/\sigma^2}, \quad (2)$$

where σ , the radial velocity dispersion, controls the disc’s dynamical temperature, $q = q(\sigma)$, and C is a normalisation constant. Finally, to mimic the disc’s inner bulge and make the disc’s total mass finite, we also introduce an inner and an outer tapering in the distribution, as detailed in appendix A.2.

The present study is motivated by the work of Sellwood (2012, hereafter S12) and Fouvry et al. (2015, hereafter F+15) which investigated a particular razor-thin model of this family (see appendix A.2 for detailed parameters). S12 used N -body simulations, while F+15 implemented BL. Let us now revisit their main result before delving further.

2.2. Sellwood (2012)’s N -body results

S12 performed long-term simulations of a razor-thin Mestel disc, limiting themselves solely to the $\ell = 2$ fluctuations. In their figure 2, S12 showed that, albeit initially stable, the disc becomes linearly unstable, and that the time at which the instability sets in depends on the number of particles, N . To prove that the disc was indeed unstable at late times, S12 stopped the simulations at different times, and restarted them after reshuffling the stars’ orbital phases. Even if this killed, de facto, any coherent bisymmetric feature, the disc was still developing a clear instability (figure 5 therein). The later the reshuffling, the stronger the instability.

Such a transition from a stable to an unstable distribution cannot be explained by linear theory. It necessarily involves changing the disc’s mean DF. When looking at the distribution of orbits in action space, S12 reported on (i) a localised depletion

¹ To ease the numerics, we soften equation (1) with $r/R_0 \rightarrow \sqrt{(r/R_0)^2 + \epsilon^2}$, with $\epsilon \ll 1$. We checked that this softening had no impact on our predictions.

of circular orbits (or groove) before the instability kicks in (figure 10 therein); (ii) the presence of a strong, sharp ridge at resonance with the instability before it saturates (figure 8 therein). The groove generated during the step (i) is responsible for the nascent instability in step (ii) (Sellwood & Kahn 1991; De Rijcke et al. 2019b).

More recently, Sellwood (2020) confirmed that their result were left unchanged when changing the N -body code from a polar to a Cartesian grid. Different individual realisations were also giving similar evolution tracks for the fluctuations.² The slow growth of the fluctuations during the onset of relaxation was still to be explained.

2.3. Fouvry et al. (2015)’s results

F+15 investigated S12’s disc by running their own numerical simulations as well as by implementing the corresponding kinetic theory. With their simulations, F+15 showed that (i) the disc’s early relaxation happens on a timescale proportional to N ; (ii) increasing the disc’s active fraction, ξ (equation A.2), accelerates the relaxation, in a non-linear fashion. Then, implementing the inhomogeneous BL equation (3), F+15 found that relaxation of the DF predicted by BL was qualitatively consistent with the measurement in one N -body simulation, exhibiting a ridge in action space. Importantly, they emphasised how collective amplification considerably reshapes the properties of the relaxation.

Taken together, S12 and F+15 offer a convincing picture for the long-term evolution of razor-thin discs. Initially stable, the disc first evolves under the collisional effects of swing amplified finite- N fluctuations. This long-term relaxation is characterised by a strong heating and churning (Sellwood & Binney 2002) of circular orbits. Ultimately, the new DF becomes linearly unstable allowing for an exponential growth of fluctuations.

Yet, a few potential caveats in this story can be raised and deserve further investigation.

1. The ridge presented in S12’s simulation is measured when the instability is already present. This ridge might not correspond to the initial change in the DF but rather be induced by a new instability. Measurements at earlier time (see S12, figure 10 therein) show a much broader depletion of circular orbits.
2. BL (equation 3) predicts the mean evolution of the DF averaged over different realisations. BL does not predict the evolution of a single (quiet start) N -body realisation, i.e., what was measured by S12.
3. The agreement between S12’s N -body measurements and F+15’s prediction is more qualitative than quantitative. The predicted ridge and the measured one are not at the same location nor with a precisely matching amplitude.

Let us now rely on recent improvements to numerical kinetic theory and our own set of N -body simulations to elucidate these elements.

² In both cases, the initial conditions were from a “quiet start” (Debatista & Sellwood 2000; Sellwood 2024). It would be interesting to investigate whether such non-Poisson-like initial conditions can bias the disc’s long-term relaxation.

3. Long-term evolution

3.1. Balescu–Lenard equation

The long-term relaxation of self-gravitating stellar systems driven by finite- N fluctuations is governed by the inhomogeneous BL equation (Heyvaerts 2010; Chavanis 2012). It reads

$$\frac{\partial F(\mathbf{J}, t)}{\partial t} = -\pi(2\pi)^d m \frac{\partial}{\partial \mathbf{J}} \cdot \left[\sum_{\mathbf{k}, \mathbf{k}'} \mathbf{k} \int d\mathbf{J}' \underbrace{U_{\mathbf{k}\mathbf{k}'}^d(\mathbf{J}, \mathbf{J}', \mathbf{k}, \boldsymbol{\Omega})^2}_{\text{dressed coupling}} \right] \times \underbrace{\delta_D(\mathbf{k} \cdot \boldsymbol{\Omega} - \mathbf{k}' \cdot \boldsymbol{\Omega}')}_{\text{resonance condition}} \underbrace{\left(\mathbf{k}' \cdot \frac{\partial}{\partial \mathbf{J}'} - \mathbf{k} \cdot \frac{\partial}{\partial \mathbf{J}} \right)}_{\text{friction}} \underbrace{F(\mathbf{J}, t) F(\mathbf{J}', t)}_{\text{orbital population}}, \quad (3)$$

with $\boldsymbol{\Omega} = \boldsymbol{\Omega}(\mathbf{J})$, the vector of orbital frequencies, and similarly $\boldsymbol{\Omega}' = \boldsymbol{\Omega}(\mathbf{J}')$. This is the master equation of self-induced orbital relaxation. This non-linear equation describes how the mean orbital population distribution $F(\mathbf{J}, t)$, with \mathbf{J} the action (appendix A.1), evolves through the correlated effects of Poisson noise, i.e., finite- N effects (with $m \propto 1/N$ the stars' individual mass). Importantly, equation (3) conserves mass, energy, and satisfies an H -theorem for Boltzmann entropy (Heyvaerts 2010). It captures the small but cumulative effects of resonant encounters between stars, whose efficiency is dressed by collective effects. The sum and the integral in this equation scan over the discrete resonances, $(\mathbf{k}, \mathbf{k}')$, and over the orbital space, $\int d\mathbf{J}'$, looking for all the possible populated resonances. These resonances are selected through the resonance condition, $\mathbf{k} \cdot \boldsymbol{\Omega} - \mathbf{k}' \cdot \boldsymbol{\Omega}' = 0$.

In equation (3), the efficiency of a given resonant coupling is set by the dressed coupling coefficients, $U_{\mathbf{k}\mathbf{k}'}^d$. These coefficients encompass all the details of linear response theory. This is briefly reviewed and validated in appendix C. As the upcoming sections show, these coefficients play an extremely important role in defining the disc's relaxation. Once linear response is under control, one may proceed with the evaluation of the BL relaxation rate, as detailed in appendix D. Naturally, the dynamics of the Mestel disc can also be investigated using N -body simulations. We detail our setup in appendix B.

3.2. Dynamical phase transition

As a first inspection of this disc's evolution, we present in figure 1, the time evolution of bisymmetric fluctuations in the disc, as observed in N -body simulations. In that figure, different lines correspond to different realisations of the same disc, i.e., they only differ in their initial conditions. First, we can note that for $t \lesssim 200 t_{\text{dyn}}$, the evolution of the discs seems rather smooth and quiescent. This is a phase of ‘‘collisional evolution’’, driven by finite- N fluctuations and described by BL. During this period, the DF changes with time but remains dynamically (Vlasov) stable. Then, for $t \gtrsim 200 t_{\text{dyn}}$, the DF becomes dynamically (Vlasov) unstable because of the groove formation, the discs change of evolution regime, and the growth of the fluctuations becomes much more rapid. The discs have gone through a dynamical phase transition toward instability (see, e.g., Campa et al. 2008, for similar behaviour in another long-range interacting system). Finally, we note that the dispersion among the different realisations gets much larger as the phase transition is approached. In figure 2, we illustrate one disc simulation in these two regimes.

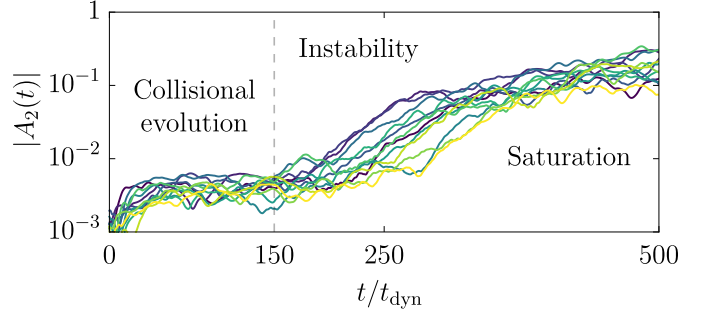


Fig. 1. Time evolution of the bisymmetric fluctuations (equation B.6) in 12 different N -body realisations of the Mestel disc, with $N = 25 \times 10^6$ particles each, using a running average over 30 dynamical times. The disc is initially stable and slowly relaxes towards an unstable state. Once unstable, the evolution is dominated by an exponentially growing mode before it saturates. The disc's configuration is illustrated in figure 2. Interestingly, the dispersion among realisations greatly increases close to the instability. The dashed line at $t/t_{\text{dyn}} = 150$ is the time at which the changes in the DF are measured in figure 3.

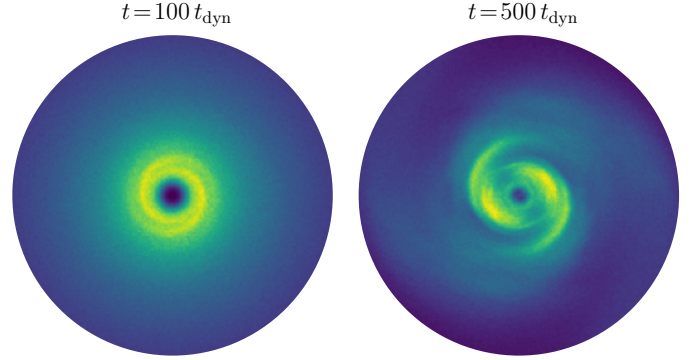


Fig. 2. Illustration of the typical evolution of a Mestel disc in one N -body simulation, via the surface density (up to $R = 8R_0$) at two different times. During the collisional phase (left), the disc remains reasonably axisymmetric, displaying recurrent weak transient spirals. After the phase transition (right), the disc develops strong bisymmetric fluctuations, which ultimately saturate (figure 1), up to the late formation of a bar (see figure 10 in F+15).

3.3. Ensemble-averaged relaxation rate

Let us now focus on the first stage of evolution and consider the averaged relaxation rate in action space, $\partial F(\mathbf{J}, t)/\partial t$, at the time $t = 150 t_{\text{dyn}}$. This is what we present in figure 3, one of the main results of the present work. In that figure, we compare the BL prediction of the relaxation rate (top panel) with the ensemble-averaged relaxation rate measured in N -body simulations. As expected, we recover that discs are heated up by resonant encounters, and orbits diffuse from quasi-circular orbits to more eccentric ones. We find that the kinetic prediction and the N -body measurements are in quantitative agreement. Both approaches predict similar shape for the relaxation rate in action space, and, importantly, with similar amplitude. Using the same criterion as in equation (12) of Tep et al. (2022), we find that $\int d\mathbf{J} F |\partial F/\partial t|$ agrees within 10% between both panels. This is an important validation of BL.

To conclude, figure 4 presents slices of figure 3 through action space. These slices show that the qualitative agreement seen in figure 3 is indeed quantitative. Indeed, the amplitude of the BL predictions falls within the distribution of simulated relaxation

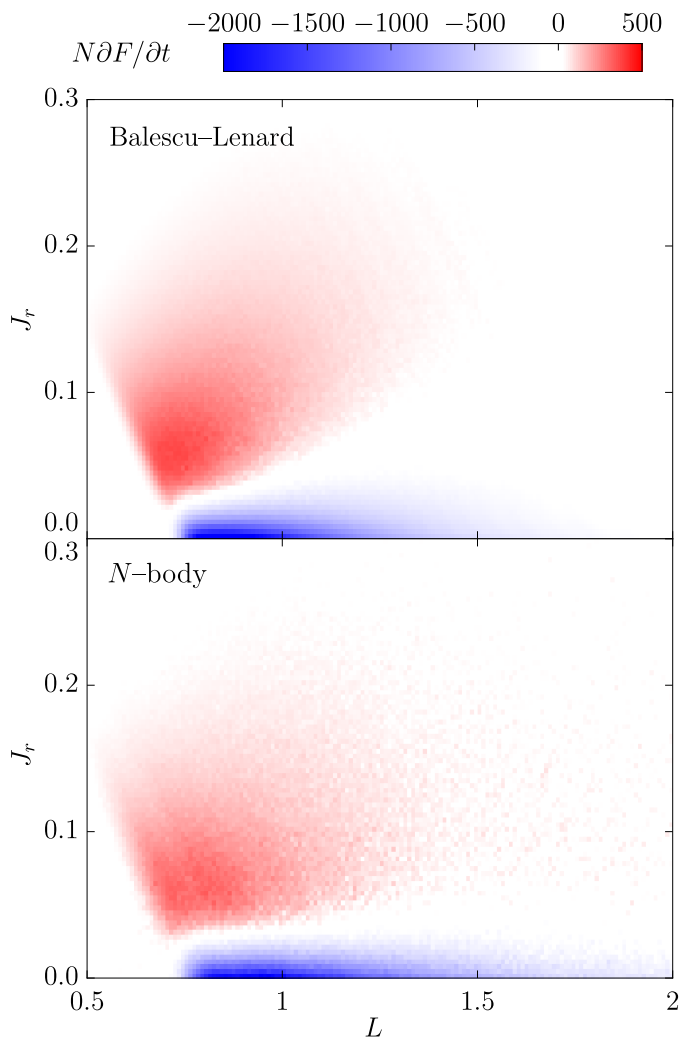


Fig. 3. *Top:* Local relaxation rate, $\partial F/\partial t$, in action space as predicted by BL (equation 3) for the Mestel disc (section 2.1), computed in the centre of the action bins. Red regions correspond to an increase in the number of particles while blue contours correspond to a depletion. *Bottom:* Relaxation rate measured in N -body simulations of the same disc, averaged over 1 000 realisations with $N = 25 \times 10^6$ particles each. The changes in the DF are computed at $t/t_{\text{dyn}} = 150$, safely before the discs become unstable (figure 1). The prediction and measurement are in good agreement, both in shape and amplitude. Slices in action space are illustrated in figure 4. Collective effects play a crucial role in shaping the long-term evolution of razor-thin discs.

rates. This figure also highlights the large spread in the relaxation rate already visible in figure 1. Such an agreement between BL and N -body simulations was definitely not a given. Indeed, the present discs are close to being marginally stable. This corresponds to a dynamical regime where strong collective amplification via the contributions from damped modes may have a significant impact on long-term relaxation (see, e.g., Hamilton & Heinemann 2020).

4. Discussion

Following figure 3, one could be tempted to conclude that BL effectively predicts the initial evolution of razor-thin self-gravitating discs, and to consider the matter settled. However, a closer examination reveals significant discrepancies between the

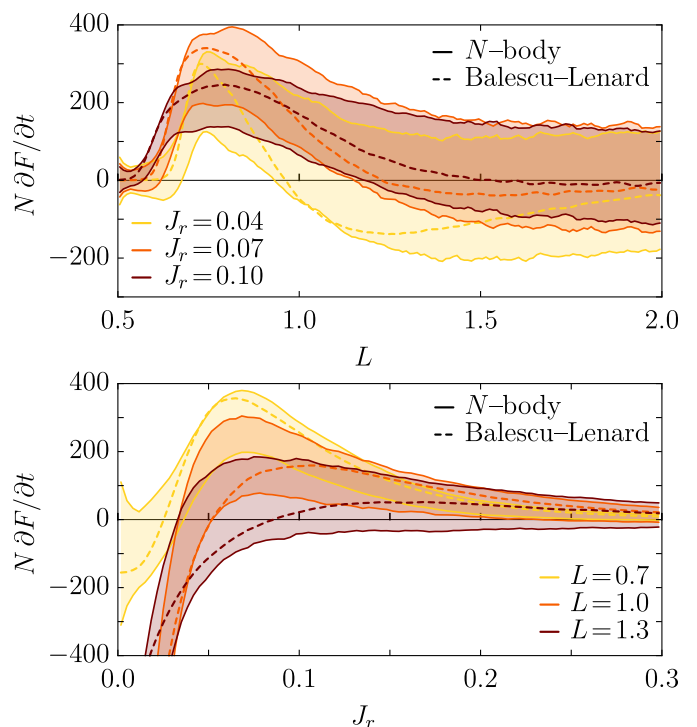


Fig. 4. Slices of the local relaxation rate, $\partial F/\partial t$, from figure 3 for fixed J_r (top) or fixed L (bottom), as predicted from BL (dashed) and measured in N -body simulations (full lines). Here, $\partial F/\partial t$ in the top (resp. bottom) panel has been averaged over an interval of width $\delta J_r = \pm 0.02$ (resp. $\delta L = 0.06$) and subsequently smoothed with a running average of width $\delta L = 0.03$ (resp. $\delta J_r = 0.01$). For the N -body, we measured $\partial F/\partial t$ in each realisation independently, estimated the standard deviation among the sample of realisations, and represented the level lines one standard deviation away from the mean value.

results of S12, F+15, and our findings. Specifically, the timing of linear instability in figure 1 and the shape of the flux in figure 3 deserve further scrutiny. Indeed, let us point out that the ensemble-averaged predictions as well as measurements from figure 3 present rather broad signatures in action space. These differ from the sharp ridge-like features presented in S12’s N -body simulation or in F+15’s BL prediction. Furthermore, the overall amplitude of the flux is yet to be convincingly explained.

To explore these issues, let us now address the following questions: (i) what is the long-term impact of collective effects? (ii) What role do (weakly) damped modes play in this long-term evolution? (iii) Does softening have any long-term signatures? (iv) How similar is an individual disc to the ensemble average? We investigate these questions in order.

4.1. Neglecting collective effects

In dynamically hot systems, i.e., systems with large velocity dispersions, collective effects can be neglected. Then, BL reduces to the Landau equation (see Chavanis 2013, and references therein). As detailed in appendix F, this amounts to replacing in equation (3) the dressed susceptibility coefficients, $U_{\mathbf{k}\mathbf{k}'}^{\text{d}}$, with their bare counterpart, $U_{\mathbf{k}\mathbf{k}'}$. Figure 5 presents the relaxation rate in action space, as predicted by the inhomogeneous Landau equation. There are two main takeaways from this figure.

First, as already pointed out by F+15, the BL relaxation rate is larger than the Landau one by three orders of magnitude. Phrased differently, collective effects considerably ac-

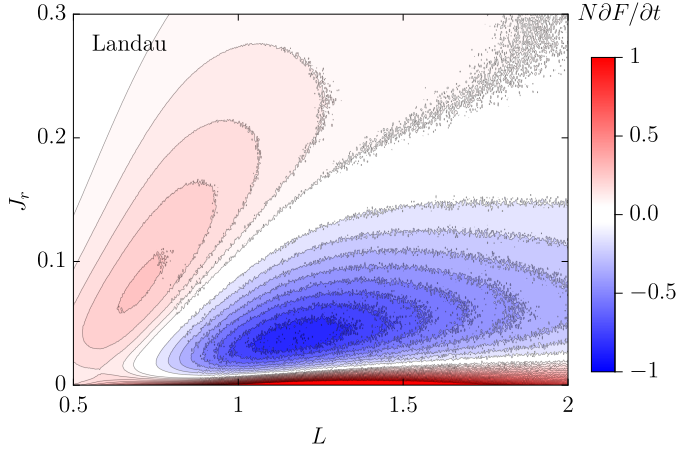


Fig. 5. Relaxation rate, $\partial F/\partial t$, as predicted by the Landau equation (see appendix F), using the same convention as in figure 3. The Landau equation predicts a more isotropic diffusion. In addition, the relaxation time predicted by BL is three orders of magnitude shorter than the one predicted by Landau: collective amplification is instrumental.

celerate the relaxation. In the present half-mass Mestel disc ($Q=1.5$), Toomre (1981) has shown that collective effects can swing amplify (Goldreich & Lynden-Bell 1965; Julian & Toomre 1966) perturbations by a factor $|U_{\mathbf{k}\mathbf{k}'}^{\mathbf{d}}/U_{\mathbf{k}\mathbf{k}'}| \simeq 30$ (figure 7 therein). Since BL involves the dressing squared, i.e., $|U_{\mathbf{k}\mathbf{k}'}^{\mathbf{d}}|^2$, this leads to a considerable acceleration of the relaxation. One gets $|\partial_t F^{\text{BL}}|/|\partial_t F^{\text{Landau}}| \simeq |U_{\mathbf{k}\mathbf{k}'}^{\mathbf{d}}/U_{\mathbf{k}\mathbf{k}'}|^2 \simeq 10^3$.

Second, we note that the BL relaxation rate (figure 3) presents much sharper structures in action space compared to the Landau one (figure 5). Yet, both kinetic equations are inhomogeneous and account for resonant encounters. We argue that the narrower features predicted by BL stem from the imprint of the disc’s weakly damped modes. These modes drive strong localised responses in the disc. This is what we explore in the next section.

4.2. Weakly damped modes

To understand the role played by (weakly) damped modes we illustrate, in figure 6, the BL relaxation rate on top of the disc’s linear susceptibility. Figure 6 is an intricate figure, that we now describe carefully.

Figure 6 is composed of two panels, each of them with two sub-plots. In both panel, the top plot is the BL relaxation rate in action space, using the same convention as in figure 3. The bottom plot represents the disc’s susceptibility, through the determinant of the susceptibility matrix, $|\mathbf{N}(\omega)|$ (equation C.5). A mode corresponds to a (complex) frequency, ω , such that $|\mathbf{N}(\omega)|$ diverges, i.e., they appear as poles in this panel. Yet, here, we do not represent the susceptibility in frequency space, but rather translate $\text{Re}[\omega]$ into an action through the circular angular momentum of the associated inner Lindblad resonance (ILR). More precisely, to any $\text{Re}[\omega]$, we can unambiguously associate an angular momentum, L , by solving

$$\mathbf{k}_{\text{ILR}} \cdot \boldsymbol{\Omega}(J_r=0, L) = \text{Re}[\omega], \quad (4)$$

with the resonance vector $\mathbf{k}_{\text{ILR}} = (k_{\text{ILR}}^r, k_{\text{ILR}}^\phi) = (-1, 2)$. With this convention, if a (quasi-circular) orbit resonates with the mode through its ILR, then the location of the orbit in action space will lie just above the associated mode in the susceptibility plot.

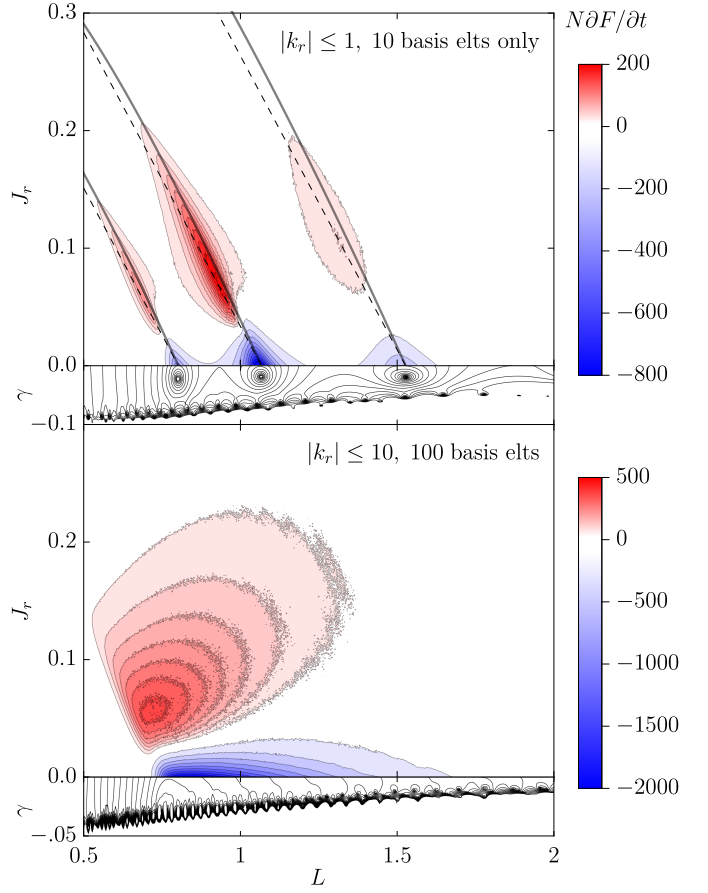


Fig. 6. Illustration of the connexion between a disc’s long-term relaxation and the disc’s linear damped modes. In each panel, we represent in the top plot the relaxation rate in action space, predicted by BL, using the same convention as in figure 3. In the bottom plot, we represent the disc’s susceptibility, $|\mathbf{N}(\omega)|$ (equation C.5) represented at the circular angular momentum corresponding to their ILR (see equation 4). The numerical saturation of the susceptibility for damped frequencies, $\gamma < 0$, is to be expected (see, e.g., Appendix B in Petersen et al. 2024). *Top:* Prediction purposely using too small a number of basis elements (appendix C.1) and too few resonances, for illustration purposes. In that case, the disc’s susceptibility contains three clear damped modes. These modes have a direct signature in the BL relaxation rate. The black line corresponds to the ILR resonance line associated with each mode while the dashed lines correspond to the direction of diffusion. The proximity of these two lines enhances the efficiency of ILR for heating the disc. *Bottom:* Same as above, but using a numerically converged linear susceptibility, namely using the same parameters as in figure 3. In both figures, we show that the disc’s long-term heating is strongly enhanced at resonance with the underlying weakly damped modes.

In figure 6, the two panels correspond to the same disc model but use different calculations of the linear susceptibility. The top panel uses, purposely, a reduced number of basis elements (appendix C.1), hence degrading the convergence of the linear predictions. This allows for the physical processes at play here to appear more clearly. The bottom panel uses the same parameters as in figure 3, with a much larger number of basis elements. It therefore relies on a converged estimation of the linear susceptibility.

Let us now focus on the top panel of figure 6. In that degraded case, the linear calculation predicts (at least) three weakly damped modes. In the associated BL prediction, one notes that each of these modes is at the origin of a sharp resonant ridge

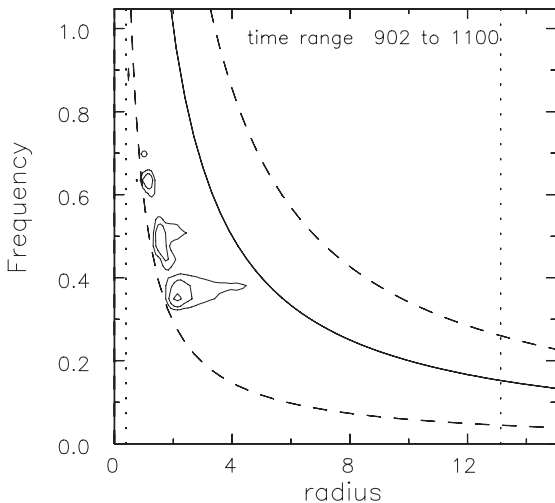


Fig. 7. Figure from S12. Power-spectra of the $\ell=2$ fluctuations as a function of radius in their N -body simulation. The presence of three peaks in these early power-spectra, and their location at their respective ILR, is likely the resonant signature of weakly damped modes.

in action space. More precisely, the real part of the mode’s frequency dictates the position of the induced ridge in action: the larger the mode’s pattern speed, the further in the resonant ridge appears. The imaginary part of the mode’s frequency dictates the width of the induced ridge in action space: the faster the mode’s damping, the wider the imprint of the ridge in action space. Overall, we note that the resonant signatures of the damped modes, because they drive such a strong collective amplification, fully dominate the long-term relaxation predicted by BL.

The same mechanism is operating in the bottom panel of figure 6. In this case, the disc’s linear susceptibility along the real axis is large within a broad frequency region, and does not display sharp signatures of distinguishable damped modes (given the shapes of the isocontours). This, in turn, drives significant amplification across a wide range of angular momenta, resulting in the broader heating in action space predicted by BL. As a consequence, BL does not exhibit distinct ridges in action space. Naturally, it would be highly valuable to refine our current implementation of linear response theory to overcome the numerical saturation evident in figure 6 and gain a clearer understanding of the modal structure of the Mestel disc.

Orbits that resonate with a mode through their ILR flow in action space along the direction of \mathbf{k}_{ILR} . Phrased differently, these orbits are heated toward more eccentric orbits with smaller guiding radii. It is worth noting that, coincidentally for the ILR, this direction of diffusion aligns closely with the associated resonance line, i.e., the line of constant $\mathbf{k}_{\text{ILR}} \cdot \boldsymbol{\Omega}(\mathbf{J})$ (black line in the top panel of Fig. 6). This alignment makes the ILR a particularly efficient resonance for heating the disc.

Interestingly, S12 observed the local power spectrum of fluctuations in their N -body simulations, before any instability has kicked in. Their resulting figure 4 is reproduced here in figure 7. In that figure, three peaks can be observed in the power spectrum, each corresponding to its respective ILR radius. These peaks are possibly associated with weakly damped modes excited by Poisson shot noise. While their number appears tentatively comparable to our results, any such comparison should be approached with caution. Indeed, the prediction in the top panel of figure 6 was degraded for illustration purposes. Obviously, improving the convergence of the linear predictions is necessary for more quan-

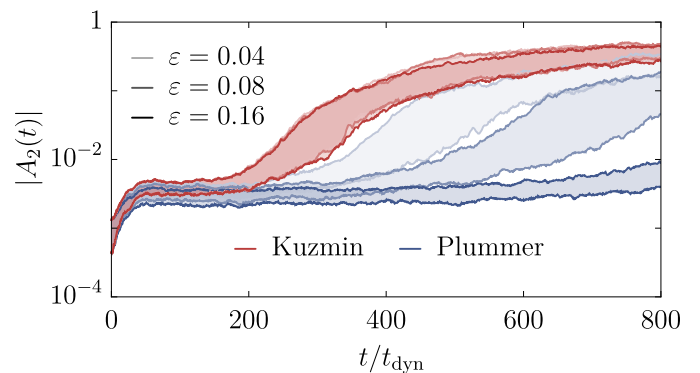


Fig. 8. Same as figure 1 but for various softening lengths, ε , and two different softening kernels (appendix G). The level of transparency correspond to different softening lengths (equation G.1) with the bottom (resp. top) line corresponding to 20% (resp. 80%) contours over 100 independent realisations with $N=25 \times 10^6$ particles. The case ‘Kuzmin $\varepsilon=0.16$ ’ corresponds to figure 1. For the Plummer kernel, the larger the softening length, the slower the relaxation, and the more delayed the transition to instability. This kernel introduces a strong gravitational bias (figure G.1). On the contrary, simulations using the Kuzmin kernel behave similarly across softening lengths. Interestingly, we note that, in every case, the dispersion among realisations increases near phase transition.

titative comparisons. In addition, one could also experiment with the method from Weinberg (1994); Heggie et al. (2020) to track damped modes in N -body simulations.

Finally, let us briefly comment on the difference between the BL prediction from F+15 (figure 4 therein) and our current BL prediction (figure 3). In F+15, BL predicted a single sharp ridge in action space, whereas, in the present work, BL predicts broader heating in action space. Since the BL’s prediction is closely tied to the accuracy of the linear susceptibility, the discrepancy between these two studies stems from the computation of the dressed coupling coefficients, $U_{\mathbf{k}\mathbf{k}'}^{\text{d}}$, which were badly converged in F+15. Appendix E details the improved methodology used in the present work to compute these coefficients more accurately.

4.3. Impact of softening

In appendix G, following De Rijcke et al. (2019a), we investigate how softening affects the complex frequency of growing modes in an unstable disc. In particular, in figure G.1, we show that Plummer softening (equation G.2) tends to shift unstable modes toward smaller pattern speed and growth rates. As a consequence, if the same trend also applies to damped modes, we expect that the stronger the softening, the faster the damping of the modes. Rephrased using the insight from figure 6, we expect that the stronger the softening, (i) the later the action space ridges should appear, (ii) the more these ridges would move toward higher angular momenta. We set out to investigate these trends in N -body simulations.

In figure 8, we illustrate the long-term evolution of bisymmetric fluctuations in N -body simulations for the two softening kernels presented in appendix G with different values of the softening length, ε . In that figure, it is clear that, for the Plummer softening kernel, increasing ε delays the phase transition toward instability. We claim that this is so because softening affects the collisionless properties of the disc, and consequently its collisional dressed resonant relaxation. Phrased differently,

(Plummer) softening makes the disc more linearly stable than it should be. Consequently, softening reduces swing amplification and ultimately delays relaxation.³

The trend from figure 8 also explains the difference in the time of phase transition between S12’s simulation and ours. Indeed, in figure 2 of S12, the instability sets in at $t \simeq 1\,200\,t_{\text{dyn}}$ using the Plummer softening with $\varepsilon = 0.125$ and $N = 50 \times 10^6$. In our case (figure 8), using $N = 25 \times 10^6$, the instability sets in at $t \simeq 400\,t_{\text{dyn}}$ (resp. 800) for the Plummer softening with $\varepsilon \simeq 0.08$ (resp. 0.16). Once accounting for the rescaling by the factor $1/N$, these timescales are nicely consistent.

We conclude this section by stressing the importance of accounting for the bias introduced by softening when comparing N -body simulations with both linear response and kinetic theory. In figure 3, we carefully chose a softening kernel, namely Kuzmin softening (equation G.3), so that the corresponding bias is small. Indeed, this kernel affects much less the disc’s linear response (see figure G.1), so that varying the softening length does not bias their long-term relaxation (figure 8).

4.4. Long-term stochasticity

BL predicts the ensemble-averaged evolution, i.e., averaged over different initial conditions drawn from the same DF. It is also of interest to investigate the dispersion that may exist among different realisations of the same disc. To do so, we represent in figure 9 the relaxation rate measured in twelve independent simulations whose fluctuations are presented in figure 1.

From figure 9, one can undoubtedly note that individual realisations are very different from the averaged one (figure 3). Indeed, on the ensemble-averaged figure, all the circular orbits ($0.75 \lesssim L \lesssim 1.5$) are depopulated in profit of more eccentric orbits. Yet, in individual realisations, the changes in the DF are much more localised, and concentrated along one or multiple sharp ridges in action space. These ridges come in different number, locations, and at different time/amplitude in each realisation.⁴ We also note that their individual intensity is up to 2-3 time larger than the averaged one.

BL is, by design, unable to predict such a diversity. Predicting the scatter among realisations could be addressed within the context of large deviation theory (see, e.g., Feliachi & Bouchet 2022). However, the inclusion of collective effects in this context is still an open question (Feliachi & Fouvry 2024). As such, the details of the processes responsible for this long-term stochasticity are still to be understood.

5. Conclusion

We presented applications of the BL kinetic theory to the self-induced long-term evolution of razor-thin self-gravitating discs. We showed that the inhomogeneous BL equation (3) is able to quantitatively predict the mean long-term evolution of these systems. The kinetic predictions were successfully compared with N -body simulations averaged over many realisations (figure 3). Doing so, we highlighted the importance of resonant encounters and collective effects in driving the relaxation of stellar discs.

³ The same trend with softening would also happen if the disc’s relaxation was driven by two-body local encounters (Theis 1998). However, such local contributions are absent from our experiments, since our simulations are, by design, limited to $\ell = 2$ fluctuations.

⁴ We note that S12 and F+15 focused on a single realisation and did not perform an ensemble average.

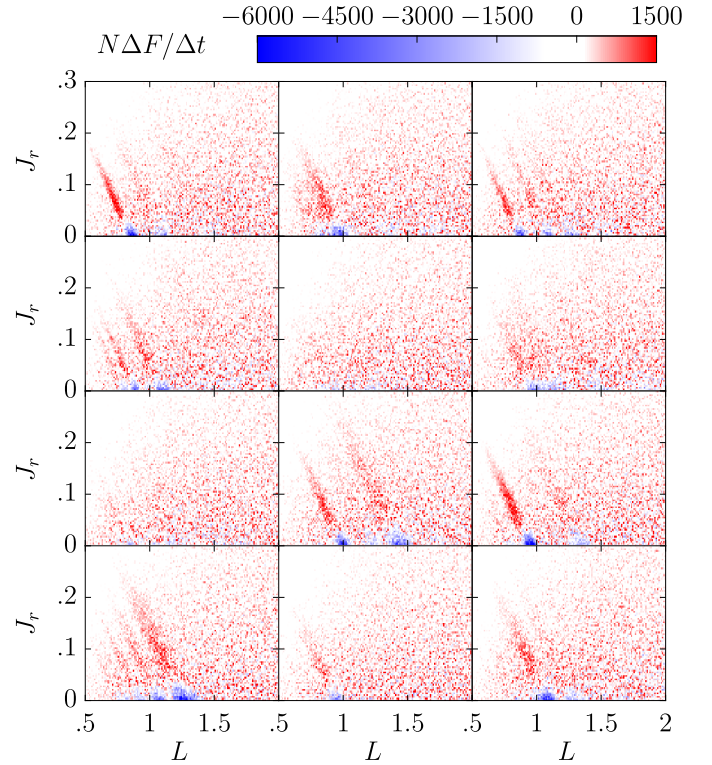


Fig. 9. Relaxation rate, $\partial F/\partial t$, measured in twelve independent N -body realisations, using the same convention as in figure 3. The number, location, amplitude and birth time of the action ridges vary strongly from one realisation to the other. This is a measure of a long-term stochasticity in the vicinity of the phase transition (see also figure 4).

The consequences of self-gravity proved to be particularly diverse (figure 5) and would have been difficult to predict *a priori* without the valuable insights provided by BL.

In these marginally stable systems, fluctuations get strongly swing amplified by resonating with the disc’s underlying weakly damped modes (figure 6). The disc’s long-term evolution is therefore particularly sensitive to the collisionless linear response of the disc. By stabilizing the disc, we showed that softening delays the phase transition to instability (figure 8). We also showed that the choice of softening kernel was critical: in razor-thin discs, the Plummer softening should be avoided both for linear and long-term responses to compare with (non-softened) theoretical predictions. Finally, we noted that, in this regime, the average relaxation rate is not representative of the individual realisations. As the disc nears marginal stability, the variance among realisations gets increasingly large (figure 9). In that sense, “the average cold galaxy does not exist”.

Let us conclude with a few prospects worth exploring to further our theoretical understanding of the long-term evolution of self-gravitating discs.

Small scale vs large scale – BL diverges on small scales (see, e.g., Chavanis 2013). Chandrasekhar (1943) did regularise the deflections at small scales taking hard encounters into account. This regularisation should be adapted to the resonant kinetic theories (see, e.g., Fouvry et al. 2021), therefore weighing the respective impact of small vs large scales on long-term relaxation. In (cold) razor-thin galactic discs, the long-range dressing by collective effects is likely to dominate, but this remains to be accurately quantified.

Time evolution – A direct follow-up of this work would involve integrating BL forward in time, beyond the onset of relaxation. Yet, integrating these equations is challenging (Weinberg 2001). There are two main difficulties to overcome: (i) computing the resonant diffusion coefficients; (ii) determining the self-consistent potential (and actions) as the disc evolves. One potential approach is to integrate the corresponding stochastic Langevin equation (see, e.g., Hénon 1971; Cohn 1979; Giersz 1998; Fu et al. 2024). This could ultimately serve to validate N -body codes on longer timescales.

Crossing marginal stability – BL unrealistically diverges at marginal stability (Weinberg 1993), though we showed here that BL is still accurate relatively close to the phase transition. Yet, if one was to evolve BL in time, it would inevitably break at some point. This divergence must be regularised by considering mode-particle interactions, in the spirit of the so-called quasi-linear theory in plasma physics (see, e.g., Rogister & Oberman 1968; Hamilton & Heinemann 2020, 2023).

Non-linear regime – After the phase transition, the disc’s evolution is dominated by the emerging unstable mode. As this mode grows, non-linear contributions become increasingly important, up to the point of saturation and trapping at resonances (see, e.g., Hamilton 2024). Investigating this late-time non-linear regime is an interesting venue.

Beyond average predictions – As highlighted in figure 9, near marginal stability the variance among different realisations increases tremendously. Predicting this scatter is crucial to assess the likelihood of a given realisation. This is beyond the reach of BL, but large deviation theory offers promising perspectives (see, e.g., Bouchet 2020; Feliachi & Bouchet 2022; Feliachi & Fouvry 2024). Ultimately, this should pave the way for the comparison of theoretical predictions of the scatter with observations and cosmological simulations.

Thick discs – Of course, the models studied here are not perfect representation of genuine galactic discs. While the case of spherically symmetric systems is well captured by BL (Roziér et al. 2019; Fouvry et al. 2021; Tep et al. 2022), the extension to thick discs or flattened spheres is yet to be achieved beyond the WKB approximation (Fouvry et al. 2017). One of the potential issue in these systems is the possible lack of integrability (see, e.g., Weinberg 2015) beyond the Stäckel family (Tep et al. 2024).

Coupled halo-disc evolution – We assumed that the disc was embedded within a static, rigid dark matter halo. Yet, the dark matter halo, albeit dynamically hotter, is also subject to fluctuations. Accounting for the coupling between the disc and the halo should provide a more realistic picture of the long-term evolution of galaxies (see, e.g., Johnson et al. 2023).

Impact of morphological type – The present analysis focussed on the Mestel disc. It would be of interest to study the efficiency of orbital diffusion on more realistic exponential disc models (see, e.g., De Rijcke et al. 2019b) while varying, e.g., the bulge to disc mass, when scanning late galaxy types of the Hubble sequence (Reddish et al. 2022).

Open dissipative systems – Finally, galaxies are not isolated objects. The Milky Way is for instance continuously perturbed by external sources triggering various response features (see, e.g., Grion Filho et al. 2021, for a review) that operate concurrently in open systems. In addition, the accounting of dissipative processes within the baryonic component can drive unlikely evolutionary pathways, possibly leading to self-regulation (Pichon 2023). This should also be the topic of future work.

Data Distribution

The data underlying this article is available through reasonable request to the author. The code for the diffusion coefficient, written in `julia` (Bezanson et al. 2017), is available at the following URL: <https://github.com/MathieuRoule/SecularResponse.jl>. The N -body code is also publicly available (courtesy of John Magorrian) at <https://github.com/MathieuRoule/mestel2d>.

Acknowledgements

This work is partially supported by grant Segal ANR-19-CE31-0017 of the French Agence Nationale de la Recherche, and by the Idex Sorbonne Université. This research was supported in part by grant NSF PHY-2309135 to the Kavli Institute for Theoretical Physics (KITP). We are grateful to J. Barré, E. Donghia, S. Flores, E. Ko, J. Magorrian, M. Petersen, K. Tep, and M. Weinberg for constructive comments. We thank J. Magorrian for providing us with his code, and Stéphane Rouberol for the smooth running of the Infinity cluster, where the simulations were performed.

References

- Aarseth, S. J. 1963, *MNRAS*, 126, 223
 Benetti, F. P. C. & Marcos, B. 2017, *Phys. Rev. E*, 95, 022111
 Bezanson, J., Edelman, A., Karpinski, S., & Shah, V. B. 2017, *SIAM Review*, 59, 65
 Binney, J. & Tremaine, S. 2008, *Galactic Dynamics: Second Edition* (Princeton Univ. Press)
 Bouchet, F. 2020, *J. Stat. Phys.*, 181, 515
 Campa, A., Chavanis, P.-H., Giansanti, A., & Morelli, G. 2008, *Phys. Rev. E*, 78, 040102
 Chakrabarty, D. 2004, *MNRAS*, 352, 427
 Chandrasekhar, S. 1943, *ApJ*, 97, 255
 Chavanis, P.-H. 2012, *Physica A*, 391, 3680
 Chavanis, P.-H. 2013, *A&A*, 556, A93
 Chavanis, P.-H. 2024, *Eur. Phys. J. Plus*, 139, 51
 Clutton-Brock, M. 1972, *Ap&SS*, 16, 101
 Cohn, H. 1979, *ApJ*, 234, 1036
 De Rijcke, S., Fouvry, J.-B., & Dehnen, W. 2019a, *MNRAS*, 485, 150
 De Rijcke, S., Fouvry, J.-B., & Pichon, C. 2019b, *MNRAS*, 484, 3198
 Debattista, V. P. & Sellwood, J. A. 2000, *ApJ*, 543, 704
 Dehnen, W. 2001, *MNRAS*, 324, 273
 Earn, D. J. D. & Sellwood, J. A. 1995, *ApJ*, 451, 533
 Eilers, A.-C., Hogg, D. W., Rix, H.-W., & Ness, M. K. 2019, *ApJ*, 871, 120
 Evans, N. W. & Read, J. C. A. 1998, *MNRAS*, 300, 106
 Feliachi, O. & Bouchet, F. 2022, *J. Stat. Phys.*, 186, 22
 Feliachi, O. & Fouvry, J.-B. 2024, *Phys. Rev. E*, 110, 024108
 Fouvry, J.-B. & Bar-Or, B. 2018, *MNRAS*, 481, 4566
 Fouvry, J.-B., Hamilton, C., Roziér, S., & Pichon, C. 2021, *MNRAS*, 508, 2210
 Fouvry, J.-B., Pichon, C., Chavanis, P.-H., & Monk, L. 2017, *MNRAS*, 471, 2642
 Fouvry, J.-B., Pichon, C., Magorrian, J., & Chavanis, P.-H. 2015, *A&A*, 584, A129
 Fouvry, J.-B. & Prunet, S. 2022, *MNRAS*, 509, 2443
 Fu, Y., Angus, J. R., Qin, H., & Geyko, V. I. 2024, *arXiv*, 2410.12079
 Gaia Collaboration et al. 2016, *A&A*, 595, A2
 Gardner, J. P., Mather, J. C., et al. 2006, *Space Sci. Rev.*, 123, 485
 Giersz, M. 1998, *MNRAS*, 298, 1239
 Goldreich, P. & Lynden-Bell, D. 1965, *MNRAS*, 130, 125
 Grion Filho, D., Johnston, K. V., Poggio, E., et al. 2021, *MNRAS*, 507, 2825
 Hamilton, C. 2024, *MNRAS*, 528, 5286
 Hamilton, C. & Heinemann, T. 2020, *arXiv*, 2011.14812
 Hamilton, C. & Heinemann, T. 2023, *MNRAS*, 525, 4161
 Heggie, D. C., Breen, P. G., & Varri, A. L. 2020, *MNRAS*, 492, 6019
 Hénon, M. 1971, *Ap&SS*, 14, 151
 Hernquist, L. & Ostriker, J. P. 1992, *ApJ*, 386, 375
 Heyvaerts, J. 2010, *MNRAS*, 407, 355
 Hunt, J. A. S., Bub, M. W., Bovy, J., et al. 2019, *MNRAS*, 490, 1026
 Johnson, A. C., Petersen, M. S., Johnston, K. V., & Weinberg, M. D. 2023, *MNRAS*, 521, 1757
 Julian, W. H. & Toomre, A. 1966, *ApJ*, 146, 810
 Kalnajs, A. J. 1976, *ApJ*, 205, 745

- Kuhn, V., Guo, Y., Martin, A., et al. 2024, *ApJ*, 968, L15
Lynden-Bell, D. & Kalnajs, A. J. 1972, *MNRAS*, 157, 1
Magorrian, J. 2007, *MNRAS*, 381, 1663
Merritt, D. 1996, *AJ*, 111, 2462
Mestel, L. 1963, *MNRAS*, 126, 553
Miller, R. H. 1971, *Ap&SS*, 14, 73
Petersen, M. S., Roule, M., Fouvry, J.-B., Pichon, C., & Tep, K. 2024, *MNRAS*, 530, 4378
Pichon, C. 2023, KITP (Santa Barbara), doi:10.26081/K6BD50
Polyachenko, E. V. 2013, *Astro. Lett.*, 39, 72
Reddish, J., Kraljic, K., Petersen, M. S., et al. 2022, *MNRAS*, 512, 160
Rogister, A. & Oberman, C. 1968, *J. Plasma Phys.*, 2, 33
Roule, M., Fouvry, J.-B., Pichon, C., & Chavanis, P.-H. 2022, *Phys. Rev. E*, 106, 044118
Rozier, S., Fouvry, J. B., Breen, P. G., et al. 2019, *MNRAS*, 487, 711
Salo, H. & Laurikainen, E. 2000, *MNRAS*, 319, 393
Sellwood, J. A. 2012, *ApJ*, 751, 44
Sellwood, J. A. 2014, *Rev. Mod. Phys.*, 86, 1
Sellwood, J. A. 2020, *MNRAS*, 492, 3103
Sellwood, J. A. 2024, *MNRAS*, 529, 3035
Sellwood, J. A. & Binney, J. J. 2002, *MNRAS*, 336, 785
Sellwood, J. A. & Evans, N. W. 2001, *ApJ*, 546, 176
Sellwood, J. A. & Kahn, F. D. 1991, *MNRAS*, 250, 278
Tep, K., Fouvry, J.-B., & Pichon, C. 2022, *MNRAS*, 514, 875
Tep, K., Pichon, C., & Petersen, M. S. 2024, *arXiv*, 2412.15033
Theis, C. 1998, *A&A*, 330, 1180
Toomre, A. 1981, in *Structure and Evolution of Normal Galaxies*, 111
Trick, W. H., Coronado, J., & Rix, H.-W. 2019, *MNRAS*, 484, 3291
Weinberg, M. D. 1993, *ApJ*, 410, 543
Weinberg, M. D. 1994, *ApJ*, 421, 481
Weinberg, M. D. 2001, *MNRAS*, 328, 311
Weinberg, M. D. 2015, *arXiv*, 1508.06855
Zang, T. A. 1976, PhD thesis, Massachusetts Institute of Technology

Appendix A: Razor-thin disc

Appendix A.1: Angle-action coordinates

Axisymmetric razor-thin discs are integrable, i.e., appropriate angle-action coordinates can explicitly be constructed for them (Lynden-Bell & Kalnajs 1972). In practice, we follow the same approach as in the library `OrbitalElements.jl`, whose main conventions we recall here (see appendix A1 in PR+24).

Orbits in a razor-thin disc can be equivalently labelled by their energy and angular momentum, (E, L) , their action (J_r, L) – with J_r the radial action, or with their pericentre and apocentre, (r_p, r_a) (see equations A1–A3 in PR+24). Orbits are skimmed with frequencies $(\Omega_r, \Omega_\phi) = (\alpha\Omega_0, \alpha\beta\Omega_0)$, with Ω_0 some frequency scale. The frequency ratios (α, β) readily follow from the angle-action mapping (see equation A4 in PR+24). Following appendix A1.1 in PR+24, all angular integrals are performed using the so-called ‘‘Hénon anomaly’’, with additional interpolations to handle extreme orbits, e.g., exactly circular or radial orbits.

Appendix A.2: Distribution function

The DF of the Mestel disc from equation (2) satisfies (equation 4.163 in Binney & Tremaine 2008)

$$q = \left(\frac{V_0}{\sigma}\right)^2 - 1, \quad C = \frac{V_0^2}{2q/2+1\pi^{3/2}G\Gamma[\frac{q+1}{2}]\sigma^{q+2}R_0^{q+1}}. \quad (\text{A.1})$$

In order to deal with the central singularity and the disc’s infinite mass, we follow Evans & Read (1998) and introduce an inner and outer tapering in the DF, leaving the mean potential unchanged. The total potential is then generated by (i) an inert bulge, (ii) an inert halo and (iii) the self-gravitating disc. In addition, one may vary the overall amplitude of the DF with the active fraction ξ . This acts as a proxy for the relative masses of the disc and its surrounding halo. The disc’s DF reads

$$F(E, L) = \xi C L^q e^{-E/\sigma^2} T_{\text{in}}(L) T_{\text{out}}(L). \quad (\text{A.2})$$

In this equation, the tapers read

$$T_{\text{in}}(L) = \frac{L^\nu}{(R_{\text{in}}V_0)^\nu + L^\nu}, \quad T_{\text{out}}(L) = \frac{(R_{\text{out}}V_0)^\mu}{(R_{\text{out}}V_0)^\mu + L^\mu}. \quad (\text{A.3})$$

The sharpness of the inner (resp. outer) taper is controlled by the power index ν (resp. μ) while its location is set by the radius R_{in} (resp. R_{out}). The outer taper was introduced by Evans & Read (1998), and is mandatory in N -body simulations to ensure that the disc is of finite mass.

The exact set of parameters we used are the same as in S12 and F+15. More precisely, in figure 3, we take $G = R_0 = V_0 = 1$ and use these units throughout the paper. We also imposed $\xi = 0.5$ (half-mass disc), $\epsilon = 10^{-5}$ for the potential truncation (see footnote 1), and fixed the tapers to $R_{\text{in}} = 1$, $R_{\text{out}} = 11.5$, $\mu = 5$, and $\nu = 4$. Finally, we set the disc’s velocity dispersion to $q = 11.4$. The value of q slightly differs between S12 ($q = 11.44$) and F+15 ($q = 11.4$). In practice, this only changes the velocity dispersion by 0.1% and we checked that it did not impact our predictions. S12’s value had a simple motivation: having nominal Toomre’s factor $Q = 1.5$.

Appendix B: N -body simulations

To perform our N -body simulation, we adapted the particle-mesh code used in F+15 (courtesy of John Magorrian), a simpler

Distribution function	Normalisation C_{sp}/C	Total mass M_{tot}	Rejection constant M
Mestel	$\simeq 9.25 \times 10^{-2}$	$10.8 (\times \xi)$	15.7
Zang $\nu = 4$	$\simeq 9.33 \times 10^{-2}$	$10.7 (\times \xi)$	11.8

Table B.1. Constants used for the sampling of the DFs from equation (B.1). The total mass M_{tot} is not set to one and corresponds to the mass enclosed within the truncation radius R_{max} (equation B.2). The individual mass of the particles is set to $m = M_{\text{tot}}/N$. The (minimal) rejection constants correspond to the maximal value of the density of state in (r_p, r_a) from equation (B.3).

2D version of the GROMMET code (Magorrian 2007). We refer to section 5.1 of F+15 for a detailed description of the code. The N -body code is publicly available (courtesy of John Magorrian) at <https://github.com/MathieuRoule/mestel2d>.

Appendix B.1: Sampling

Improving upon appendix E of F+15, we sample the DF from (A.2) in (r_p, r_a) -space rather than in (E, L) -space. Let us briefly detail our approach.

Following equation (A.2), we need to sample the DF

$$F_{\text{sp}}(E, L) = C_{\text{sp}} L^q e^{-E/\sigma^2} T_{\text{in}}(L) T_{\text{out}}(L), \quad (\text{B.1})$$

complemented with the truncation constraint⁵

$$r_a(E, L) \leq R_{\text{max}}. \quad (\text{B.2})$$

In equation (B.1), the constant C_{sp} ensures that F_{sp} is normalised to unity when integrated w.r.t. $dx dv$. We report the values used in table B.1.

The constraint from equation (B.2) imposes that the populated domain in the (r_p, r_a) -space is a triangle. Accounting carefully for the Jacobian of the transformation $(J_r, L) \rightarrow (r_p, r_a)$, the density of state in (r_p, r_a) is

$$p(r_p, r_a) = \frac{(2\pi)^2}{\Omega_r} \left| \frac{\partial(E, L)}{\partial(r_p, r_a)} \right| F_{\text{sp}}(E, L), \quad (\text{B.3})$$

where the $(2\pi)^2$ factor comes from integrating over the angles, and the Jacobian $|\partial(E, L)/\partial(r_p, r_a)|$ is computed using `OrbitalElements.jl` (PR+24).

To sample $p(r_p, r_a)$, we use a rejection sampling against the uniform distribution

$$g(r_p, r_a) = \frac{2}{R_{\text{max}}^2} \mathbb{1}_{\{0 \leq r_p\}} \mathbb{1}_{\{r_p \leq r_a\}} \mathbb{1}_{\{r_a \leq R_{\text{max}}\}},$$

with the rejection constant M satisfying

$$\forall (r_p, r_a), \quad p(r_p, r_a) \leq \frac{2M}{R_{\text{max}}^2}. \quad (\text{B.4})$$

The values used for this rejection constant are given in table B.1.

⁵ As in F+15, we interpret this constraint as ‘‘no particles with orbits that extend beyond $R_{\text{max}}F(E, L) = 0$ when $E > \psi_{\text{eff}}(R_{\text{max}})$ [and not $\psi(R_{\text{max}})$, see S12].

Appendix B.2: Measuring fluctuations and modes

Let us now describe our method to measure the fluctuation's strength (figures 1 and 8) and to estimate the frequency and growth rate of the dominant mode in N -body simulations of unstable discs (appendix G). We follow an approach similar to appendix C in F+15.

Considering that the system's density fluctuations are well described by a single dominant mode, they read

$$\delta\rho(\mathbf{r}, t) = \rho_M(\mathbf{r}) \exp(i\omega_M t), \quad (\text{B.5})$$

with ρ_M the shape of the mode and ω_M its (complex) frequency. The density fluctuation can be projected on any spatial function, $f(\mathbf{r}) = f(r) e^{i\ell\phi}$, to give

$$A_\ell(t) = \int d\mathbf{r} f(\mathbf{r}) \delta\rho(\mathbf{r}, t) = m \sum_{i=1}^N f[r_i(t)] e^{i\ell\phi_i(t)}, \quad (\text{B.6})$$

From the time series $t \rightarrow A_\ell(t)$, one expects then the behaviour

$$|A_\ell(t)| \propto e^{\gamma_M t}; \quad \arg[A_\ell(t)] \propto \Omega_M t, \quad (\text{B.7})$$

provided one ‘‘unwraps’’ the phases. In figure B.1, we illustrate such time series for an unstable Mestel disc (namely, Zang's $\nu=4$ disc, Zang 1976). To measure the dominant mode's frequency, we use the log-normal function

$$f(r) = \exp\left[-\frac{\ln(r/R_0)^2}{2\sigma^2}\right], \quad (\text{B.8})$$

with $r_0 = 1.33$ and $\sigma = 0.45$. This mimics the radial shape of the mode, hence easing the measurement. If one uses multiple functions for the projections, one could also estimate the mode's shape.

To investigate long-term evolution of fluctuations in figures 1 and 8, we use the simpler identity function

$$f(r) = \mathbb{1}(r_{\min} < r < r_{\max}), \quad (\text{B.9})$$

with $(r_{\min}, r_{\max}) = (1.5 r_0, 4.5 r_0)$. This removes the contributions from the disc's central and outer regions, where very few particles are present.

Appendix B.3: Measuring the relaxation rate

To measure the BL relaxation rate in numerical simulations (figure 3), we performed 1000 realisations of the Mestel disc, each with $N = 25 \times 10^6$ particles. We used the Kuzmin softening (equation G.3) with $\varepsilon = 0.16$ sufficiently small so that the gravitational bias is negligible (see figure G.1). For the numerical integration, we used a leapfrog scheme with timestep $\delta t = 10^{-2} t_{\text{dyn}}$. The forces are estimated using a Cartesian grid that extends to $\pm x_{\max} = 20$ with $n_x \times n_y = 1024^2$ cells. The $\ell=2$ fluctuations are selected using the same method as in section 5.1 of F+15, with a polar grid of $n_r = 8192$ radial rings and $n_\phi = 2048$ points in the azimuthal direction.

For post-processing, we use `OrbitalElements.jl` to compute the particles' actions (J_r, L) within the mean potential from equation (1). We count their number, $n(J_i, L_j)$, in bins of width $\delta J_r = 1/300$, $\delta L = 1/100$. From these bin counts, the DF and its changes are obtained through

$$n(J_i, L_j) \simeq (2\pi)^2 \frac{N}{M_{\text{tot}}} \delta J_r \delta L F(J_i, L_j),$$

where the $(2\pi)^2$ prefactor comes from the integration over $d\theta_r d\theta_\phi$. To estimate $\partial F / \partial t$ in figure 3, we computed the difference between $t = 150 t_{\text{dyn}}$ and $t = 0$.

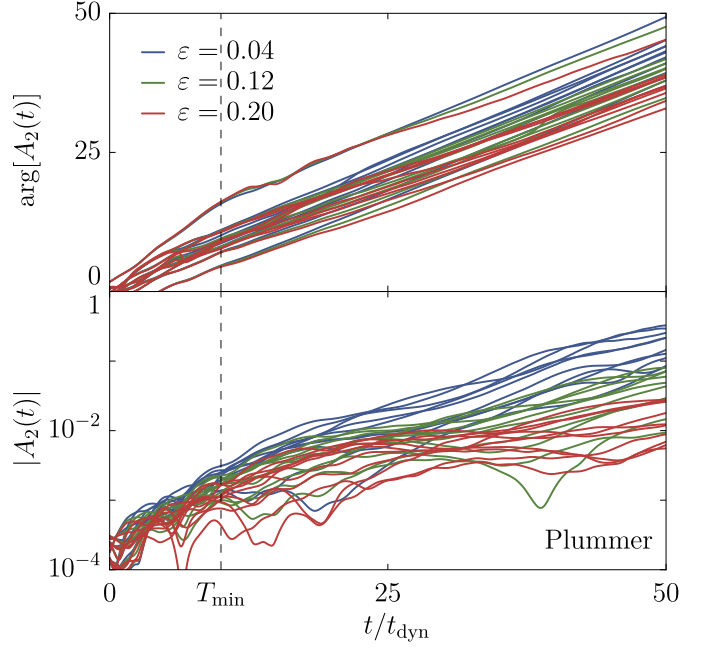


Fig. B.1. Time series of the unwrapped phase (top) and the norm (bottom) of the bisymmetric fluctuations probed by $A_2(t)$ from equation (B.6) over 10 independent realisations of the unstable Zang $\nu=4$ disc (Zang 1976). Each simulation is performed with $N = 2 \times 10^8$ particles using the Plummer softening kernel (equation G.2) and for varying softening lengths, ε . For each ε , the same ten initial conditions are used and shown in the same colour. The frequency Ω_M (resp. growth rate γ_M) of the mode are estimated by a linear fit of the phase (resp. log of the norm) of such time series, only using $t \geq T_{\min} = 10 t_{\text{dyn}}$. The growth of the phase is generically more regular than the growth of the norm. The Plummer softening kernel introduces a strong gravity bias.

Appendix C: Linear response theory

As shown in equation (3), collective effects play a critical role in shaping the long-term relaxation of dynamically cold systems. Therefore, it is essential to handle the numerical aspects of linear response theory with precision. To do so, we use the publicly available library `LinearResponse.jl` (PR+24) and its associated dependencies. In this section, we briefly outline the main building blocks of this calculation.

Appendix C.1: Biorthogonal bases

Following the convention from `AstroBasis.jl` (PR+24), we introduce a basis of potential-density pairs

$$\psi^{(p)}(\mathbf{w}) = \int d\mathbf{w}' \rho^{(p)}(\mathbf{w}') U(\mathbf{w}, \mathbf{w}') \quad (\text{C.1a})$$

$$\int d\mathbf{w} \psi^{(p)}(\mathbf{w}) \rho^{(q)*}(\mathbf{w}) = -\delta_{pq}, \quad (\text{C.1b})$$

with $U = -G/|\mathbf{r} - \mathbf{r}'|$ the gravitational potential. From these basis elements, the interaction potential takes the pseudo-separable form (Hernquist & Ostriker 1992)

$$U(\mathbf{w}, \mathbf{w}') = - \sum_p \psi^{(p)}(\mathbf{w}) \psi^{(p)*}(\mathbf{w}'). \quad (\text{C.2})$$

In the present case, the disc's axisymmetry entices us to introduce basis elements of the form $\psi^{(p)}(r, \phi) = U_p^\ell(r) e^{i\ell\phi}$ with $U_p^\ell(r) \in \mathbb{R}$. In practice, we use the radial basis elements

from Clutton-Brock (1972) available in `AstroBasis.jl`. Advantageously, this basis is (i) global (one only has to set one scale radius); (ii) has infinite extent; (iii) can be computed via a numerically-stable recurrence relation.

Appendix C.2: Response matrix

Linear response is generically captured by the response matrix $\mathbf{M}(\omega)$ (see, e.g., equation 5.94 in Binney & Tremaine 2008) whose elements generically read

$$M_{pq}(\omega) = -(2\pi)^d \sum_{\mathbf{k} \in \mathbb{Z}^d} \int d\mathbf{J} \frac{\mathbf{k} \cdot \partial F / \partial \mathbf{J}}{\mathbf{k} \cdot \boldsymbol{\Omega}(\mathbf{J}) - \omega} \psi_{\mathbf{k}}^{(p)*}(\mathbf{J}) \psi_{\mathbf{k}}^{(q)}(\mathbf{J}), \quad (\text{C.3})$$

with the Fourier transformed basis elements

$$\psi_{\mathbf{k}}^{(p)}(\mathbf{J}) = \frac{1}{(2\pi)^d} \int d\boldsymbol{\theta} e^{-i\mathbf{k} \cdot \boldsymbol{\theta}} \psi^{(p)}(\mathbf{w}), \quad (\text{C.4})$$

The definition from equation (C.3) holds as such only for $\text{Im}(\omega) > 0$. It must be analytically continued to the rest of the complex plane (see, e.g., Fouvry & Prunet 2022).

From the response matrix, one defines the susceptibility matrix, $\mathbf{N} = [\mathbf{I} - \mathbf{M}(\omega)]^{-1}$. The *dressed* coupling coefficients then read (see, e.g., equation 35 in Heyvaerts 2010)

$$U_{\mathbf{k}\mathbf{k}'}^d(\mathbf{J}, \mathbf{J}', \omega) = - \sum_{p,q} \psi_{\mathbf{k}}^{(p)}(\mathbf{J}) N_{pq}(\omega) \psi_{\mathbf{k}'}^{(q)*}(\mathbf{J}'). \quad (\text{C.5})$$

These coefficients describe how stellar orbits collectively interact with one another.

Appendix C.3: Computations parameters

To compute the response matrix used in figure 3, we used the `LinearResponse.jl` library with the same parameters as PR+24 (see tables F1 therein) which checked for convergence using the unstable Zang $\nu=4$ disc. Importantly, except when stated differently, we used 100 basis elements and summed over 21 resonances (i.e. for $|k_r| \leq 10$ in equation C.3). In the top panel of figure 6, the same parameters are used, except for the (specified) number of basis elements and resonances.

Appendix D: Balescu–Lenard equation

The Balescu–Lenard equation (equation 3) is a diffusion equation in action space. Hence, it can be rewritten as $\partial F(\mathbf{J}, t) / \partial t = -\partial / \partial \mathbf{J} \cdot \mathcal{F}(\mathbf{J})$. The associated flux, $\mathcal{F}(\mathbf{J})$, is driven by resonances so that $\mathcal{F}(\mathbf{J}) = \sum_{\mathbf{k}, \mathbf{k}'} \mathcal{F}_{\mathbf{k}\mathbf{k}'}(\mathbf{J})$ with

$$\mathcal{F}_{\mathbf{k}\mathbf{k}'}(\mathbf{J}) = \int d\mathbf{J}' G_{\mathbf{k}\mathbf{k}'}(\mathbf{J}, \mathbf{J}') \delta_D[f_{\mathbf{k}\mathbf{k}'}(\mathbf{J}, \mathbf{J}')], \quad (\text{D.1})$$

Here, we introduced the integrand

$$G_{\mathbf{k}\mathbf{k}'}(\mathbf{J}, \mathbf{J}') = \pi (2\pi)^d m \mathbf{k} \left| U_{\mathbf{k}\mathbf{k}'}^d(\mathbf{J}, \mathbf{J}', \mathbf{k} \cdot \boldsymbol{\Omega}) \right|^2 \times \left[\mathbf{k}' \cdot \frac{\partial F}{\partial \mathbf{J}'} F(\mathbf{J}) - \mathbf{k} \cdot \frac{\partial F}{\partial \mathbf{J}} F(\mathbf{J}') \right]. \quad (\text{D.2})$$

and the resonance condition $f_{\mathbf{k}\mathbf{k}'}(\mathbf{J}, \mathbf{J}') = \mathbf{k} \cdot \boldsymbol{\Omega} - \mathbf{k}' \cdot \boldsymbol{\Omega}'$.

For a fixed value of $(\mathbf{k}, \mathbf{k}', \mathbf{J})$, we must integrate along the resonance line in \mathbf{J}' given by $f_{\mathbf{k}\mathbf{k}'}(\mathbf{J}, \mathbf{J}') = f(\mathbf{J}') = 0$. To do so, we use the same resonant coordinates, (u, v) , as in appendix A1.3 of PR+24 (see also appendix B of Fouvry & Prunet

2022). We refer to these papers for definitions and notations. Within these coordinates, the resonance condition becomes

$$f(u', v') = \Omega_0 \Delta_{\mathbf{k}'} (u_{\text{res}} - u'), \quad (\text{D.3})$$

with the resonant value

$$u_{\text{res}} = \varpi_{\mathbf{k}'}(\mathbf{k} \cdot \boldsymbol{\Omega} / \Omega_0), \quad (\text{D.4})$$

where

$$\varpi_{\mathbf{k}'}(\omega) = \frac{\omega - \Sigma_{\mathbf{k}'}}{\Delta_{\mathbf{k}'}}. \quad (\text{D.5})$$

In equations (D.3–D.5), we introduced the frequency scale, $\Omega_0 = V_0 / R_0$, along with $\Sigma_{\mathbf{k}'} = \frac{1}{2}(\omega_{\mathbf{k}'}^{\text{min}} + \omega_{\mathbf{k}'}^{\text{max}})$ and $\Delta_{\mathbf{k}'} = \frac{1}{2}(\omega_{\mathbf{k}'}^{\text{max}} - \omega_{\mathbf{k}'}^{\text{min}})$, where $\omega_{\mathbf{k}'}^{\text{min}}$ (resp. $\omega_{\mathbf{k}'}^{\text{max}}$) is the minimal (resp. maximal) value reached by the (dimensionless) resonance frequency $\omega_{\mathbf{k}'} = \mathbf{k}' \cdot \boldsymbol{\Omega} / \Omega_0$. These extrema can be determined following appendix B of Fouvry & Prunet (2022). Performing the change of variables $\mathbf{J}' \rightarrow (u', v')$ in equation (D.1) and using the property $\delta_D(\alpha x) = \delta_D(x) / |\alpha|$, the flux ultimately reads

$$\mathcal{F}_{\mathbf{k}\mathbf{k}'}(\mathbf{J}) = H(u_{\text{res}}) \int_{-1}^1 \frac{dv'}{\Omega_0 \Delta_{\mathbf{k}'}} \left| \frac{\partial \mathbf{J}'}{\partial (u', v')} \right| G_{\mathbf{k}\mathbf{k}'}[\mathbf{J}, \mathbf{J}'(u_{\text{res}}, v')],$$

with the rectangular Heaviside function, $H = \mathbb{1}_{[-1,1]}$, imposing $|u_{\text{res}}| \leq 1$. In practice, we performed these integrals using the midpoint rule with 100 sampling points. Following appendices A4.1 and F of PR+24, the resonance coordinate v' is chosen to spread more evenly along the resonance line using `vmapn=2` (see equation A18 therein). The dressed coupling coefficients in the integrand, $G_{\mathbf{k}\mathbf{k}'}$ (equation D.2), are computed via equation (C.5) using 100 basis elements. The response matrix is computed with `LinearResponse.jl`, as detailed in appendix C.3.

To compute the relaxation rate in figure 3, we finally need to sum over the pairs of resonance numbers, $(\mathbf{k}, \mathbf{k}')$. For discs, symmetry imposes $k_\phi = k'_\phi = \ell$, with ℓ the considered harmonic number. In practice, following F+15, we limited ourselves to the inner Lindblad resonance $\mathbf{k} = (-1, 2)$, the outer Lindblad resonance $\mathbf{k} = (1, 2)$, and the corotation resonance $\mathbf{k} = (0, 2)$, accounting for the harmonics $\ell = \pm 2$. In practice, we also checked that increasing the number of radial resonances beyond $|k_r| = 1$ had a negligible impact on the kinetic prediction. Finally, the relaxation rate, $\partial F / \partial t$, is computed from the flux using finite differences with the step distance, $\delta J_r = \delta L = 10^{-3}$.

Appendix E: Linear response implementation

Let us list the main differences between F+15 and our work regarding the implementation of linear response: (i) F+15 used the bi-orthogonal basis from Kalnajs (1976), while we used the one from Clutton-Brock (1972). This latter basis does not suffer from numerically unstable recurrence relations. (ii) F+15 used only 9 basis functions, but did not perform any convergence check w.r.t. these parameters.⁶ In the present work, we used 100 basis elements to obtain figure 3. We also aimed to ensure the numerical convergence of the susceptibility coefficients. (iii) F+15 computed the resonant integral from equation (C.3) in pericentre and apocentre compared to our tailored resonant coordinates (see appendix A1.3 of PR+24 and appendix B of Fouvry & Prunet

⁶ For example, we checked that using the same control parameters as F+15 within `LinearResponse.jl` (Petersen et al. 2024) leads to the incorrect prediction that the half-mass Mestel disc is unstable.

2022). But, more worryingly, F+15 was not able to evaluate $U_{\mathbf{k}\mathbf{k}'}^{\text{d}}(\omega)$ for purely real frequencies, and resorted to computing it for slightly imaginary frequencies. Our use of the analytical continuation proposed by Fouvry & Prunet (2022) allowed us to explicitly circumvent this issue.

The combination of all these elements lead us to believe that the dressed coupling coefficients computed by F+15 were not converged. Since an incorrect linear response calculation can lead to an incorrect BL prediction (figure 6), the BL prediction presented in F+15 should, surely, be considered with great circospection.

Appendix F: Landau equation

In the absence of collective amplification, BL becomes the Landau equation (see, e.g., Chavanis 2013). This amounts to making the replacement $U_{\mathbf{k}\mathbf{k}'}^{\text{d}}(\mathbf{J}, \mathbf{J}', \omega) \rightarrow U_{\mathbf{k}\mathbf{k}'}(\mathbf{J}, \mathbf{J}')$ in equation (3). The bare susceptibility coefficients, $U_{\mathbf{k}\mathbf{k}'}(\mathbf{J}, \mathbf{J}')$, are the Fourier transform in angles of the pairwise interaction potential, i.e., they read

$$\begin{aligned} U_{\mathbf{k}\mathbf{k}'}(\mathbf{J}, \mathbf{J}') &= \int \frac{d\boldsymbol{\theta}}{(2\pi)^d} \frac{d\boldsymbol{\theta}'}{(2\pi)^d} U[(\boldsymbol{\theta}, \mathbf{J}), (\boldsymbol{\theta}', \mathbf{J}')] e^{-i \cdot (\mathbf{k} \cdot \boldsymbol{\theta} - \mathbf{k}' \cdot \boldsymbol{\theta}')} \\ &= - \sum_p \psi_{\mathbf{k}}^{(p)}(\mathbf{J}) \psi_{\mathbf{k}'}^{(p)*}(\mathbf{J}') \end{aligned} \quad (\text{F.1})$$

In the razor-thin axisymmetric case, we can expand the interaction potential in the polar coordinates (r, ϕ) to give

$$U([r, \phi], [r', \phi']) = \sum_{\ell} U^{\ell}(r, r') e^{i\ell(\phi - \phi')}, \quad (\text{F.2})$$

with

$$U^{\ell}(r, r') = \frac{1}{\pi} \int_0^{\pi} d\gamma U(r, r', \gamma) \cos(\ell\gamma), \quad (\text{F.3})$$

This last function can be written as

$$\begin{aligned} U_{\mathbf{k}\mathbf{k}'}^{\ell}(\mathbf{J}, \mathbf{J}') &= \frac{\delta_{k_{\phi}}^{\ell} \delta_{k'_{\phi}}^{\ell}}{\pi^2} \int_0^{\pi} d\theta_r \int_0^{\pi} d\theta'_r U^{\ell}(r, r') \\ &\quad \times \cos[k_r \theta_r + k_{\phi}(\theta_{\phi} - \phi)] \\ &\quad \times \cos[k'_r \theta'_r + k'_{\phi}(\theta'_{\phi} - \phi')], \end{aligned} \quad (\text{F.4})$$

For the gravitational case, we have

$$U(r, r', \Delta\phi) = \frac{-G}{\sqrt{r^2 + r'^2 - 2rr' \cos \Delta\phi}}, \quad (\text{F.5})$$

from which we find

$$U^{\ell}(r, r') = \frac{-G}{\bar{r}} \frac{{}_3\tilde{F}_2\left[\left(\frac{1}{2}, \frac{1}{2}, 1\right), (1-\ell, 1+\ell), 2a/(1+a)\right]}{\sqrt{1+a}}, \quad (\text{F.6})$$

where $\bar{r} = \sqrt{r^2 + r'^2}$, $a = 2rr'/\bar{r}^2$ and ${}_3\tilde{F}_2$ is the regularised (generalised) hypergeometric function. Equation (F.6) diverges for $r = r'$, but this divergence is to be integrated over through equation (F.4). In practice, to avoid numerical instabilities, we regularise the interaction potential by using the Plummer softened potential, U_{ε} (Aarseth 1963; Dehnen 2001)

$$U_{\varepsilon}(\mathbf{r}, \mathbf{r}') = - \frac{G}{\sqrt{\varepsilon^2 + \|\mathbf{r} - \mathbf{r}'\|^2}}, \quad (\text{F.7})$$

with $\varepsilon/R_0 = 10^{-5}$. Fortunately, even with softening, $U_{\varepsilon}^{\ell}(r, r')$ still follows equation (F.6) with the change $\bar{r} = \sqrt{r^2 + r'^2 + \varepsilon^2}$.

In practice, the double integral in equation (F.4) can be computed using the midpoint rule. This calculation is useful to benchmark the biorthogonal basis calculations, by comparing the two expressions from equation (F.1). Reassuringly, we find that both approaches are in satisfactory agreement with one another. In practice, we used equation (F.1) with 100 basis elements to compute the Landau prediction presented in figure 5. All the other parameters of the computation are kept the same as for the BL prediction (appendix D).

Appendix G: Softening

In N -body simulations, the Newtonian interaction potential, $U(r) = -G/r$, diverges at small separations. As a result, one typically softens the interaction potential via (Dehnen 2001)

$$U_{\varepsilon}(r) = \frac{-G}{\varepsilon} f\left(\frac{r}{\varepsilon}\right), \quad (\text{G.1})$$

with f a dimensionless kernel and ε the softening length.

The impact of softening on the stability of self-gravitating systems has been well studied (see, e.g., Miller 1971; Salo & Laurikainen 2000; Sellwood & Evans 2001; Polyachenko 2013). Typically, too much softening leads to a strong bias in the gravitational force, while too little softening leads to numerical instabilities (Merritt 1996). This is a classical bias-variance trade-off.

In that context, De Rijcke et al. (2019a) (hereafter DR+19b) investigated specifically the impact of the softening kernel on the instabilities of self-gravitating discs. In particular, DR+19b considered two softening kernels, namely the Plummer kernel⁷

$$f_{\text{P}}(u) = \frac{1}{\sqrt{1+u^2}}, \quad (\text{G.2})$$

and the (modified) Kuzmin kernel

$$f_{\text{K}}(u) = \frac{3 + \frac{5}{2}u^2 + u^4}{(1+u^2)^{5/2}}. \quad (\text{G.3})$$

Interestingly, DR+19b showed that the Plummer softening impacts the disc's unstable modes at order $\mathcal{O}(\varepsilon)$, while the Kuzmin kernel only impacts at order $\mathcal{O}(\varepsilon^2)$. This makes it a preferred kernel for the razor-thin geometry. DR+19b compared their theoretical predictions of linear instabilities with the Plummer softening against the N -body simulations of Earn & Sellwood (1995) (isochrone disc) and Sellwood & Evans (2001) (Mestel disc). A good agreement was found on the modes' frequencies.

In this Appendix, we conduct a similar investigation for the Zang $\nu=4$ disc (same as Sellwood & Evans 2001), using both the Plummer and Kuzmin kernels. The results are presented in figure G.1. On the N -body front, for each kernel and softening length, we performed 10 independent realisations with $N=2 \times 10^8$ particles each. We found that the unstable modes were indeed less affected by the Kuzmin kernel compared to the Plummer kernel. Our numerical measurements align with the predictions from DR+19b as well as the earlier results of Sellwood & Evans (2001). However, it is important to note that in this figure, the N -body errors are likely underestimated: Sellwood & Evans (2001) did not account for the scatter among different realisations, while we did not include any uncertainties in the mode fits.

⁷ This kernel mimics the effect of finite thickness (Sellwood 2014).

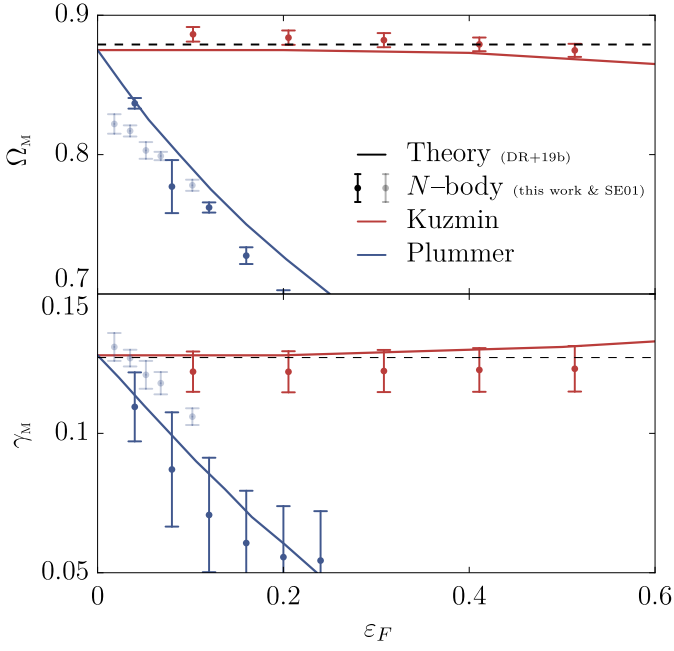


Fig. G.1. Pattern speed (top) and growth rate (bottom) of the dominant mode in Zang $\nu = 4$ disc (Zang 1976), as a function of the rescaled softening length, ε_F (equation G.5), for the Plummer softening kernel (blue – equation G.2) and the Kuzmin kernel (red – equation G.3). The theoretical predictions (plain lines) are reproduced from DR+19b (figure 3 therein), with the dashed line corresponding to the Newtonian (non-softened) prediction from Evans & Read (1998) (table D1b therein). The N -body measurements are from Sellwood & Evans (2001) (faint dots SE01 – Plummer softening only – figure 1 panel b therein), and our own measurements (plain dots – both kernels). Here, we recover that the Plummer kernel has a strong gravity bias, i.e., a predicted change in the mode’s property $\Delta\omega_M^{\text{Plummer}} \propto \varepsilon$, while the Kuzmin kernel satisfies $\Delta\omega_M^{\text{Kuzmin}} \propto \varepsilon^2$.

In figure G.1, the softening length, ε , is rescaled. Indeed, since equation (G.1) is invariant under the transformation (section 2.3 of DR+19b)

$$\varepsilon \rightarrow a\varepsilon \quad \text{and} \quad f(u) \rightarrow af(au), \quad (\text{G.4})$$

one ought to be careful when comparing softening lengths. Here, we follow DR+19b, and compare the kernels using

$$\varepsilon_F = -\varepsilon/f'_{\text{max}}, \quad (\text{G.5})$$

with f'_{max} the maximal value of the derivative of the softening (dimensionless) kernel. Setting $\varepsilon_F/\varepsilon = 1$ for the Plummer softening, one has $\varepsilon_F/\varepsilon \approx 2.568$ for the Kuzmin softening (table 1 in DR+19b).